PEGylation-Dependent Cell Uptake of Lipid Nanoparticles Revealed by Spatiotemporal Correlation Spectroscopy

Luca Digiacomo, Serena Renzi, Andrea Pirrottina, Heinz Amenitsch, Valentina De Lorenzi, Daniela Pozzi, Francesco Cardarelli,* and Giulio Caracciolo*

Cite This: https://doi.org/10.1021/acsptsci.4c00419

Read Online

ACCESS | Metrics & More | Article Recommendations | Supporting Information

ABSTRACT: Polyethylene glycol (PEG) is a common surface modification for lipid nanoparticles (LNPs) to improve their stability and in vivo circulation time. However, the impact of PEGylation on LNP cellular uptake remains poorly understood. To tackle this issue, we systematically compared plain and PEGylated LNPs by combining dynamic light scattering, electrophoretic light scattering, and synchrotron small-angle X-ray scattering (SAXS) that unveils a striking similarity in size and core structure but a significant reduction in surface charge. Upon administration to human embryonic kidney (HEK 293) cells, plain and PEGylated LNPs were internalized through different endocytic routes, as revealed by spatiotemporal correlation spectroscopy. An imaging-derived mean square displacement (iMSD) analysis shows that PEGylated LNPs exhibit a significantly stronger preference for caveolae-mediated endocytosis (CAV) and clathrin-mediated endocytosis (CME) pathways compared to plain LNPs, with these latter being better tailored to MCR-dependent internalization and trafficking. This suggests that PEG plays a crucial role in directing LNPs toward specific cellular uptake routes. Further studies should explore how PEG-mediated endocytosis impacts intracellular trafficking and ultimately translates to therapeutic efficacy, guiding the design of next-generation LNP delivery systems.

KEYWORDS: PEGylation, lipid nanoparticles, DNA delivery, nanoparticle-cell interactions, endocytic pathways
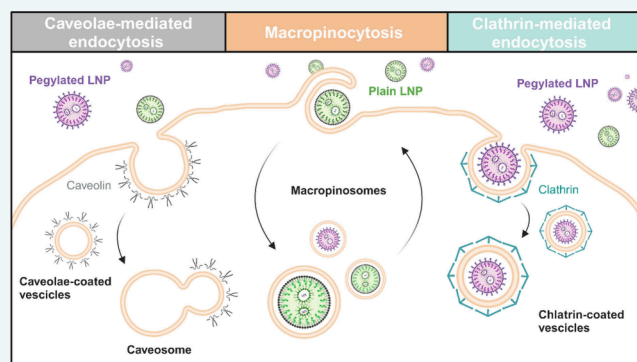
Lipid nanoparticles (LNPs) have emerged as promising vehicles for nucleic acid delivery, holding significant potential for therapeutic and biotechnological applications.[1] A key strategy in NP design involves the use of polyethylene glycol (PEG) on the surface.[2] PEGylation offers several advantages, including enhanced colloidal stability in biological fluids, reduced recognition by the immune system, and prolonged circulation time within the body.[3−8] On the other hand, several studies suggest that PEGylation can induce unexpected immune reactions[9] and decrease the cellular uptake of LNPs also by the target cells,[10−12] thus hindering LNP delivery and efficacy.[13] This latter effect is tentatively ascribed to the steric hindrance caused by the PEG layer, which may hinder the interaction between the LNP and the cell membrane. The precise impact of PEG on the cellular uptake of LNPs in terms of LNP−membrane interaction and internalization pathways remains a critical and incompletely understood issue. As an instance, it has been shown that PEGylated LNPs containing short interfering RNAs enter cells by both clathrin-mediated endocytosis and macropinocytosis, then escape from endosomes with low efficiency and only during a limited time window.[14,15] However, these results cannot be directly generalized to LNPs delivering different

biomolecules, e.g., plasmid DNA, as the payload plays a determining role in shaping the final features of LNPs (e.g., their size), their structural stability, and, in turn, their intracellular behavior. To elucidate these aspects, this study aims to systematically investigate how the presence of PEG on DNA-loaded LNPs influences cellular uptake mechanisms in human embryonic kidney cells (HEK293) by spatiotemporal image correlation spectroscopy that has emerged as a powerful alternative[16] to three-dimensional (3D) single particle tracking (SPT)[17] for investigating the trafficking mechanisms of nanoparticles in cells. In our study, we utilized an image Mean Square Displacement (iMSD) analysis derived from STCS to elucidate these mechanisms.[18] By analyzing fluctuations in fluorescence intensity over both space and time, iMSD allows for the extraction of dynamic parameters, such as local diffusivity (Dmicro, hereafter D_m), the coefficient
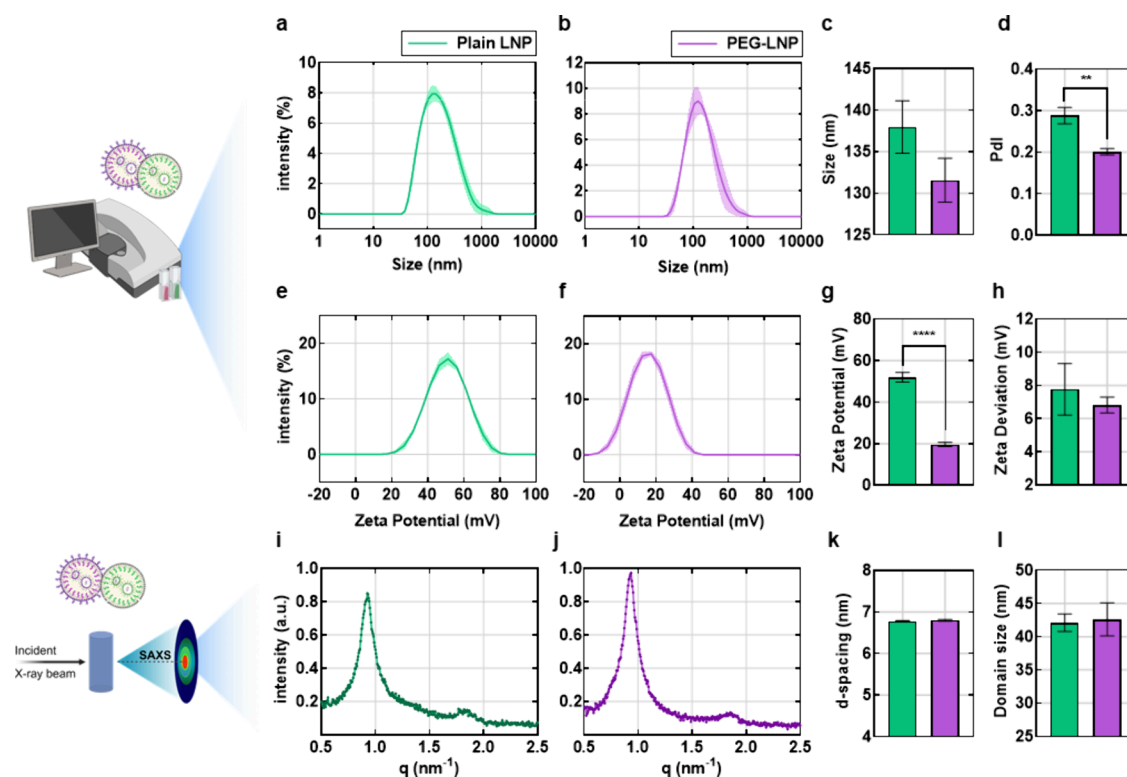
Figure 1. Chemical-physical characterization of plain and PEGylated lipid nanoparticles (LNPs). Intensity size distribution of plain (a) and PEGylated LNPs (b). Average size (c) and polydispersity index (PdI; d). Zeta potential distribution of plain (e) and PEGylated (f) LNPs. Histograms of zeta potential of plain and PEGylated LNPs from three independent measurements (g) and corresponding standard deviation (j). Synchrotron SAXS pattern of plain (h) and PEGylated (k) LNPs. Lamellar d-spacing of plain and PEGylated LNPs (i) and corresponding scattering domain size (l). The color code used is green for plain nanoparticles and purple for PEGylated nanoparticles. The size and zeta potential distributions in a, b, e, and f include shaded areas representing the standard deviation of the distributions. Statistical significance was calculated using a Student's t test, with * for $p < 0.05$, ** for $p < 0.01$, *** for $p < 0.001$, and **** for $p < 0.0001$.

of anomalous diffusion (α), and the offset parameter (σ_0^2). When represented in a parametric 3D space, this approach uniquely captures the major structures involved in endocytic processes—specifically, caveolae, clathrin-coated vesicles, and macropinosomes—by a single point corresponding to a triplet of parameters. These distributions serve as distinctive fingerprints for specific cellular pathways. By comparing the iMSD-derived parameters of plain and PEGylated LNPs to those characteristics of endocytic vesicles, we demonstrate that plain LNPs preferentially use macropinocytosis (MCR), while PEGylation diversifies particle uptake pathways to include caveolae-mediated endocytosis (CAV) and clathrin-mediated endocytosis (CME).

RESULTS AND DISCUSSION

Assigning a specific role to PEG in NP uptake mechanisms demands a comprehensive understanding of all the physicochemical parameters that can influence this process, such as size, surface charge, and nanostructure.[19] We meticulously characterized both plain and PEGylated LNPs using state-of-the-art techniques to gain a comprehensive understanding of their physicochemical properties. Figure 1 summarizes our findings.

Dynamic light scattering (DLS) reveals that both plain and PEGylated LNPs fall within the 130−140 nm size range, indicating a level of uniformity suitable for drug delivery applications. Worthy of mention, PEGylated nanoparticles displayed a lower polydispersity index (PdI), translating to

enhanced stability and predictability within biological systems. The PEG coating likely contributes to this homogeneity by minimizing aggregation and improving the solubility of the LNPs. Zeta potential measurements, on the other hand, provide insights into the colloidal stability and interaction potential. The higher cationic nature of plain particles (zeta potential ~50 mV) suggests stronger electrostatic interactions, potentially impacting cellular uptake and the biodistribution of LNPs. Conversely, the weakly cationic nature of PEGylated particles (zeta potential, ~20 mV) indicates reduced electrostatic interactions, potentially leading to lower opsonization[20] and lower removal from the bloodstream by immune cells.[21] Finally, synchrotron small-angle X-ray scattering (SAXS) characterizes the nanostructures of the LNPs. SAXS data reveal domains within the NPs sized around 45 nm with a spacing of slightly less than 7 nm, indicating a regular internal organization. According to the literature,[22,23] the multilamellar structure suggests the presence of multiple internal layers, which can influence drug-loading capacity and release kinetics.[24] Importantly, SAXS data do not highlight significant structural differences between plain and PEGylated LNPs, underscoring that PEGylation primarily affects surface characteristics rather than core structure.[25−27]

At this point, to quantitatively compare the internalization mechanisms of PEGylated and unPEGylated LNPs, we employed spatiotemporal correlation spectroscopy in the form of imaging-derived Mean Squared Displacement (iMSD) analysis (further information can be found in previous reports[28]) as detailed in Figure 2a. iMSD is a rapid and robust
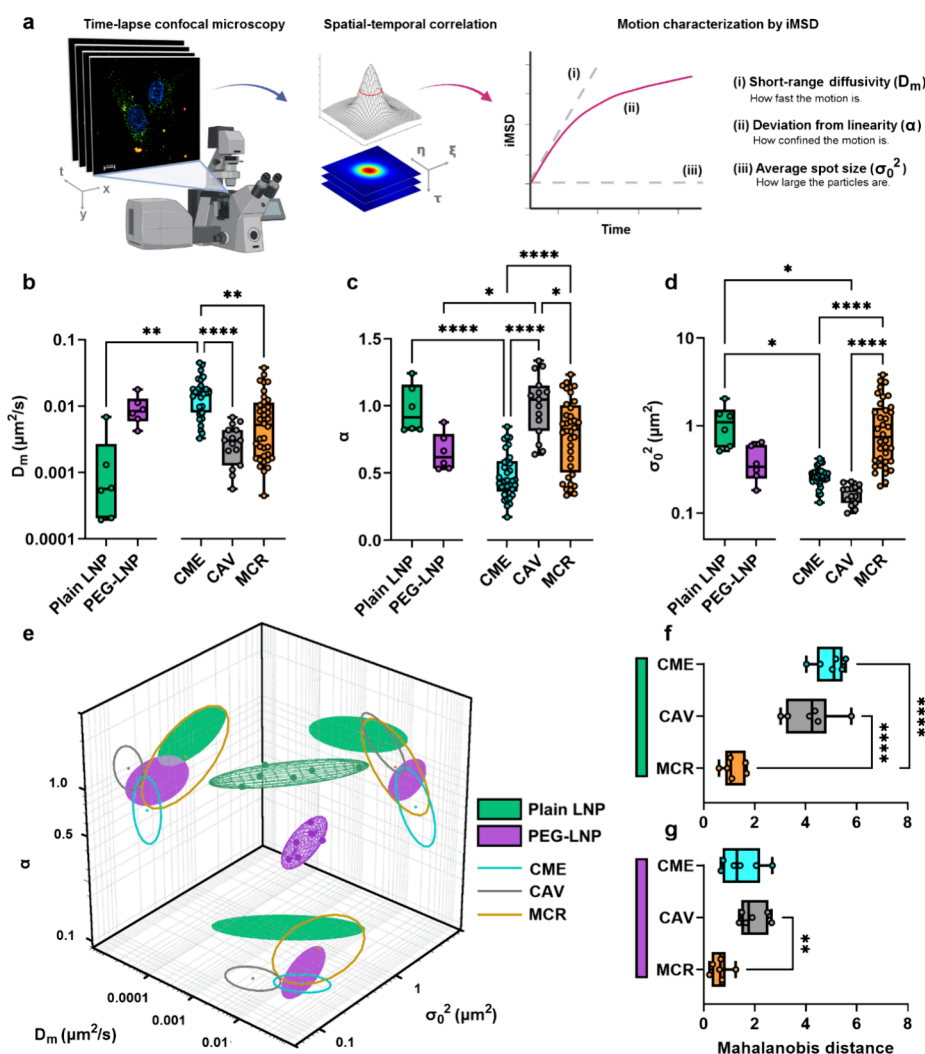
Figure 2. iMSD-based dynamic fingerprint analysis of LNPs. (a) Schematic representation of the iMSD-based dynamic fingerprint analysis. Time-lapse confocal microscopy captures a series of images of fluorescently labeled intracellular structures. The iMSD algorithm processes these images to generate the spatiotemporal correlation function (see Methods for the specific equations). Gaussian fitting of these correlation functions produces the iMSD plot. From the fitting equation, three key parameters are selected to quantitatively describe the average dynamic properties of the structure of interest: (b) the short-range diffusion coefficient (D_m), i.e., how fast the intracellular motion of LNPs is; (c) the anomalous diffusion coefficient (α), i.e., how confided the intracellular motion of LNPs is; and (d) the y-axis intercept of the iMSD plot, indicating the average size of the diffusing structures. (e) A 3D plot displays the extracted parameters for plain LNPs, PEGylated LNPs, CME, CAV, and MCR. The histograms show the Mahalanobis distances of data points for (f) plain LNPs and (g) PEGylated LNPs, in comparison to the distributions of CME, CAV, and MCR. Representative confocal image time-series for plain LNPs and PEGylated LNPs are provided as Supporting Information. Data for CME, CAV, and MCR are reproduced from ref 29. Available under a CC BY 4.0 license.

method that can afford a real-time quantitative estimate of the average size (σ^2, or offset), diffusivity (D_m), and overall mode of motion (α, or anomalous coefficient) of the population of diffusing objects with no need to reconstruct single-object trajectories. Moreover, it eliminates potential biases by not requiring prior knowledge of specific cellular structures. In brief, the process starts with rapid imaging of a designated region of interest within the cell, typically encompassing the entire cytoplasm. Subsequently, the spatiotemporal correlation function is calculated by comparing acquired images at progressively increasing time delays. As the object of interest moves, the width of the spatial autocorrelation function broadens proportionally to the time delay, quantitatively depicting the overall motion of the population of dynamic particles. Fitting the spatiotemporal correlation function allows for the extraction of the average iMSD and the related

structural and dynamic information (i.e., D_m, α, and σ_0^2). The values of these parameters are then used to build a 3D plot in which each point corresponds to a single-cell iMSD acquisition. Data from different cells form clusters in the 3D space whose position and shape define the fingerprint of the structural and dynamic properties of the diffusing object under study.

Initially, fluorescently labeled variants of crucial structures involved in endocytic processes—including clathrin-mediated endocytosis (CME), caveolae-mediated endocytosis (CAV), and macropinocytosis (MCR)—were utilized. We present the results of the iMSD analysis separately for the short-term diffusion coefficient (Figure 2b), the anomalous diffusion exponent (Figure 2c), and the intercept value (Figure 2d). These results are then integrated into a unified 3D plot (Figure 2e).

It is noteworthy that the three endocytic pathways exhibit clear distinctions based on the average characteristic size and dynamics of the involved structures, as characterized in a previous work by some of us.[29] While a direct comparison to previous electron microscopy analyses of these organelles is not possible within our data set, the retrieved σ_0^2 values align well with expected trends, showing that CAV < CME < MCR. Our analysis also reveals interesting differences in the dynamic behavior of endocytic vesicles associated with the three major pathways. CME, for instance, appears to involve structures with significantly higher local mobility compared to CAV and MCR. These structures are known to detach readily from the plasma membrane within a short time frame, becoming freely mobile within the cytoplasm.[30] By contrast, caveolae are known to reside in the plasma membrane for extended periods before internalization. Additionally, their intracellular trafficking appears to be slower compared to CME.[31]

Subsequently, these parameters were extracted for both plain and PEGylated LNPs. By correlating these parameters with the dynamic fingerprints associated with each endocytic pathway, we explored the specific mechanism through which the LNPs were internalized.

Of note, the iMSD analysis reveals distinct mobility patterns for plain and PEGylated LNPs compared to established endocytic vesicle markers. Plain LNPs exhibited significant differences in short-term diffusion coefficient compared to CME, as well as in anomalous diffusion exponent and intercept values compared to both CME and CAV. In contrast, PEGylated LNPs did not exhibit statistically significant differences in any of the measured parameters (D_m, α, σ_0^2) compared to any of the endocytic vesicle markers. To provide a quantitative estimation of this behavior, we compared multivariate distributions of LNPs and endocytic vesicles in terms of Mahalanobis distance.[32] By calculating the Mahalanobis distances for plain (Figure 2f) versus PEGylated (Figure 2g) LNPs, we could establish a statistically sound measure of how divergent their movement patterns truly are. A larger Mahalanobis distance indicates a more substantial difference in the underlying mobility characteristics, while a smaller Mahalanobis distance suggests a closer resemblance to the reference distribution. By observing the Mahalanobis distances between plain and PEGylated LNPs, we can understand how surface modifications influence their journey inside cells. The much shorter distances between PEGylated LNPs and the distributions of CAV and CME compared to plain LNPs suggest PEGylation plays a key role in triggering these specific pathways.

The observed activation of CAV for PEGylated LNP uptake is intriguing, as it challenges the commonly held belief that CAV is limited to cargos smaller than 80 nm. Recent reports highlight the complexities of definitively identifying CAV uptake, particularly due to potential artifacts arising from caveolin-1 overexpression during experimentation.[33] In light of these considerations, our data suggest a potential alternative for the interaction between PEGylated LNPs and caveolae. The internalization process may involve LNP association with the caveolar surface rather than complete encapsulation within traditional caveosomes. This surface interaction could be mediated by specific physicochemical properties of the PEGylated LNPs, potentially involving interactions between the PEGylated surface and caveolar membrane components. Further investigation, which is beyond the scope of the present

work, is necessary to elucidate the precise mechanism underlying this observed association.

As both plain and PEGylated LNPs have similar size and core chemistry, these latter properties cannot satisfactorily explain the differences in how they are taken up by the cells. On the other hand, PEGylation reduces the surface charge of LNPs. This change in surface charge may have implications for their interaction with cellular membranes and subsequent uptake mechanisms. Our findings suggest that grafting PEG to the LNP surface introduces subtle changes to the LNP surface, potentially creating docking points for CAV and CME machinery on the cell membrane. The shift in Mahalanobis distances highlights the potential effect of PEGylation in manipulating how LNPs are processed inside cells. Indeed, although the main uptake route for all the investigated LNPs was MCR, PEGylation favored primarily CME and—secondarily—CAV pathways (Figure 2f, g). Interestingly, MCR and CME have been already observed as the main uptake mechanisms of siRNA-loaded LNPs.[15] Specifically, the two processes have been reported to be interdependent with CME serving as the initial constitutive entry mechanism that triggers MCR activation in a rate-limiting manner. Although a detailed analysis of the kinetics of the process is out of the scope of this work, some considerations can be traced about the role of PEGylation in endocytic pathways. Indeed, our results suggest that PEGylation may influence crucial factors in the intracellular trafficking of LNPs, like where the LNPs travel within the cell, how they release their cargo, and, ultimately, how effective they are as a treatment. Future investigations will delve deeper into these implications by applying various complementary techniques (e.g., inhibitors of endocytic routes) and exploring different cell lines or levels of PEGylation (e.g., using different PEG lengths) to understand how PEGylation-induced activation of specific endocytic pathways affects LNP behavior inside cells and ultimately influences their therapeutic potential.

CONCLUSIONS

This study sheds light on the significant impact of surface modifications on the intracellular trafficking of LNPs. By employing a combination of physicochemical characterization and iMSD analysis, we demonstrate that PEGylation alters the interaction of LNPs with the cellular environment, favoring specific endocytic pathways. The observed shift toward CAV and CME upon PEGylation suggests a potential mechanism for manipulating the intracellular fate of LNPs. These findings hold promise for developing next-generation LNP delivery systems with optimized therapeutic efficacy by harnessing the specific properties of different endocytic pathways to enhance successful cargo release in the cytosol, while simultaneously avoiding lysosomal degradation. To this end, future investigations should explore the downstream consequences of PEGylation-induced endocytosis on factors like intracellular trafficking, payload release, and ultimately therapeutic potential.

METHODS

Materials. The zwitterionic lipids dioleoylphosphatidyl ethanol-amine (DOPE, catalog number: 850725P) and 1,2-dioleoyl-*sn*-glycero-3-phosphocholine (DOPC, catalog number: 850375P), the cationic lipids 1,2-dioleoyl-3-trimethylammonium-propane (DOTAP, catalog number: 890890P) and

(3β-[N-(N′,N′-dimethylaminoethane)-carbamoyl])-cholesterol (DC-Chol, catalog number: 700001P), and the PEG-lipid 1,2-I dioleoyl-*sn*-glycero-3-phosphoethanolamine-N-[amino-(polyethylene glycol)-2000] (DOPE-PEG 2000, catalog number: 880234P) were all sourced from Avanti Polar Lipids (Alabaster, AL). Plasmid DNA (pmirGLO, catalog number: E1330) containing the firefly luciferase reporter gene was obtained from Promega (Madison, WI, USA).

Preparation of Lipid Nanoparticles. Two different lipid nanoparticles (LNPs) were prepared using cationic and zwitterionic lipids, with one formulation including PEG-lipid and the other without. Each lipid was dissolved separately in absolute ethanol (Sigma-Aldrich, catalog number: S-32205-1L-M) at a final concentration of 25 mM. The plain formulation was created with DOTAP:DC-Chol:DOPC:DOPE in a molar ratio of 25:25:25:25. The PEGylated formulation was prepared with DOTAP:DC-Chol:DOPC:DOPE:DOPE-PEG in a molar ratio of 25:25:25:23.5:1.5. Plasmid DNA (pDNA) was diluted in 25 mM sodium acetate (pH 4) to a final concentration of 0.4 mg/mL. The lipid and DNA solutions were mixed using the NanoAssemblr Ignite microfluidic platform (Precision NanoSystems Inc., Vancouver, BC, Canada). This platform uses two syringes connected to a cartridge (Ignite NxGen) through separate inlets, where the lipid and DNA solutions are combined under controlled conditions within the thin channel on the cartridge. LNPs were assembled at a total flow rate (TFR) of 2 mL/min, with a DNA-to-lipid flow rate ratio (FRR) of 3:1. Following micromixing, the residual ethanol (25% v/v) was removed by dialysis using a cassette with a molecular weight cut off (MWCO) of 3.5 kDa (Thermo Scientific, Rockford, AZ, USA) against 400 mL of phosphate-buffered saline (PBS) at pH 7.4. The dialysis conditions were set according to the literature to ensure the complete removal of ethanol from the sample solution. After 19 h of dialysis, the LNPs were collected in a sample tube, and the final pH was measured with a pH meter.

Size and Zeta Potential Measurements. Size (reported as zeta-average) and zeta potential measurements were performed by dynamic light scattering and laser Doppler electrophoresis using a Zetasizer Nano ZS90 (Malvern, UK). Samples were diluted 1:10 with distilled water (Thermo Fisher, catalog number:15230001) for size measurements and 1:60 with distilled water for zeta potential measurements. Results are reported as the mean ± the SD of three repeated measurements.

Synchrotron SAXS Experiments. Synchrotron Small Angle X-ray Scattering (SAXS) measurements were conducted at the Austrian SAXS beamline ELETTRA (Trieste, Italy) using a Pilatus3 1 M (Dectris, Baden, Switzerland) detector calibrated with silver behenate powder (*d*-spacing = 5.838 nm). The *q* range was fixed between 0.05 and 5 nm^{-1}, with an exposure time of 10 s. The analysis included corrections for the background, primary beam intensity, and detector efficiency.

Cell Culture. The human embryonic kidney (HEK-293) cell line was obtained from ATCC (Rockville, MD, USA) and cultured in Dulbecco's Modified Essential Medium (DMEM, Thermo Fisher, catalog number: 12491015) supplemented with 10% v/v fetal bovine serum (FBS, Thermo Fisher, catalog number: 10270-106) and 1% v/v penicillin-streptomycin (Thermo Fisher, catalog number: 10378016). Cells were kept in an incubator at 37 °C with 5% CO_2 in a humidified atmosphere.

Confocal Microscopy. Live-cell imaging was performed using a Zeiss LSM 800 confocal microscope, equipped with a 63×, 1.4 N.A. oil immersion objective and GaAsP detectors. About 200,000 HEK-293 cells were seeded in a 22 mm WillCo glass bottom dish 24 h before the experiment. On the day of the experiment, cells were incubated with TexasRed (Merck, catalog number: T1395MP)-labeled PEGylated or non-PEGylated LNPs (1×) for 3 h at 37 °C. Confocal images (512 × 512 pixels, 50 nm pixel size) were taken with TexasRed excited at 561 nm (HeNe laser), and emissions were collected between 570 and 630 nm. To elucidate the specific endocytic routes involved in NP uptake, this study employed various labeling techniques for different cellular markers, as reported in previous studies.[29] For CME, cells were incubated with a 0.1 mM stock solution of transferrin conjugated to Alexa Fluor 488 (Invitrogen, catalog number: T13342) prepared in phosphate-buffered saline (PBS) for 20 min at 37 °C. Following incubation, the medium was replaced. Transferrin, a well-established ligand for CME, serves as a marker for this pathway. CAV was investigated by introducing Caveolin-E1GFP into the cells via electroporation using the Neon Transfection System 100 μL Kit (Invitrogen, catalog number: MPK10096). Briefly, 1×10^6 cells were suspended in 220 μL of Resuspension Buffer R and supplemented with 15 μg of Caveolin-E1GFP DNA. The Neon Transfection System delivered the DNA at 1005 V and a 35 ms pulse width. After transfection, cells were seeded and cultured for 24 h in DMEM (Thermo Fisher, catalog number: 12491015) supplemented with 10% FBS (Thermo Fisher, catalog number: 10270−106), excluding antibiotics, before being used in experiments. This technique utilizes Caveolin-E1GFP as a marker, because caveolin is a key structural protein in caveolae. MCR was labeled using Fluorescein isothiocyanate (FITC)-Dextran 70 kDa (Sigma-Aldrich, catalog number: 90718). Cells underwent three washes with PBS (Corning, catalog number: 21-031-CV), followed by incubation with fresh media containing Dextran (1 mg/mL) for 30 min at 37 °C. Finally, the cells were washed again, and the media were replaced. FITC-Dextran, due to its size and ability to be engulfed by large vesicles, served as a marker for macropinocytosis.

Image Mean Square Displacement analysis. For the iMSD analysis, a time series of 400 frames was recorded (256 × 256 pixels, 100 nm pixel size, 0.2 s time-lapse) and processed with custom scripts, as detailed in prior studies.[29] The spatiotemporal correlation function of the detected intensity was computed and analyzed over spatial and temporal lag variables. The Gaussian variance (σ^2) as a function of the lag time was plotted to create the iMSD curve, which was then fitted for further analysis. In detail, this curve was fitted to

$$\sigma^2(\tau) = \sigma_0^2 + K\tau^\alpha \tag{1}$$

to determine the α value, which is associated with subdiffusive (i.e., $\alpha < 1$), superdiffusive (i.e., $\alpha > 1$) motion, or Brownian diffusion (i.e., $\alpha = 1$). σ_0^2 represents the curve's intercept and is related to the average size of the fluorescent-labeled particles and the waist of the point spread function. Finally, to quantify the intracellular dynamics of the investigated systems, the iMSD curve was fitted to

$$\sigma^2(\tau) = \sigma_0^2 + 4D_M\tau + \frac{L^3}{3}\left(1 - \exp\left\{-\frac{\tau}{\tau_c}\right\}\right) \tag{2}$$

where L is the linear size of the confinement area, τ_c quantifies how fast confinement occurs, and D_M is the particle diffusivity on a large time scale. The short-term diffusivity D_m is measured by the slope of σ^2 for $\tau \to 0$ and reads $D_m = D_M + L^2/(12\tau_c)$.

The multivariate distributions of LNPs and endocytic vesicles were compared in terms of Mahalanobis distance.[32] The Mahalanobis distance is a statistical parameter representing a non-Euclidean distance between a data point and a distribution, which quantifies the deviation of an individual data point from a reference distribution within a high-dimensional space. Unlike the classical Euclidean distance, which focuses solely on the straight-line separation, the Mahalanobis distance incorporates the inherent correlations between the various parameters (e.g., diffusion coefficient and anomalous coefficient).

■ ASSOCIATED CONTENT

ⓈⅠ Supporting Information

The Supporting Information is available free of charge at https://pubs.acs.org/doi/10.1021/acsptsci.4c00419.

> Representative movie for plain LNPs (AVI)
>
> Representative movie for PEGylated LNPs (AVI)

■ AUTHOR INFORMATION

Corresponding Authors

Francesco Cardarelli − *Laboratorio NEST, Scuola Normale Superiore, 56127 Pisa, Italy;* ⓞ orcid.org/0000-0003-3049-5940; Email: francesco.cardarelli@sns.it

Giulio Caracciolo − *NanoDelivery Lab, Department of Molecular Medicine, Sapienza University of Rome, 00161 Rome, Italy;* ⓞ orcid.org/0000-0002-8636-4475; Email: giulio.caracciolo@uniroma1.it

Authors

Luca Digiacomo − *NanoDelivery Lab, Department of Molecular Medicine, Sapienza University of Rome, 00161 Rome, Italy*

Serena Renzi − *NanoDelivery Lab, Department of Molecular Medicine, Sapienza University of Rome, 00161 Rome, Italy*

Andrea Pirrottina − *NanoDelivery Lab, Department of Molecular Medicine, Sapienza University of Rome, 00161 Rome, Italy*

Heinz Amenitsch − *Institute of Inorganic Chemistry, Graz University of Technology, 8010 Graz, Austria*

Valentina De Lorenzi − *Laboratorio NEST, Scuola Normale Superiore, 56127 Pisa, Italy;* ⓞ orcid.org/0000-0002-7429-6524

Daniela Pozzi − *NanoDelivery Lab, Department of Molecular Medicine, Sapienza University of Rome, 00161 Rome, Italy*

Complete contact information is available at:
https://pubs.acs.org/10.1021/acsptsci.4c00419

Author Contributions

L.D.: data curation, formal analysis, investigation, software, validation, visualization, writing−review and editing. S.R.: data curation, formal analysis, investigation, validation, writing−review and editing. A.P.: investigation, validation, visualization. H.A.: conceptualization, methodology, validation. V.D.L.: investigation, validation. D.P.: conceptualization, project administration, resources. F.C.: conceptualization, funding acquisition, methodology, project administration, resources, supervision, writing−review and editing. G.C.: conceptualiza-tion, funding acquisition, methodology, project administration, resources, supervision, writing−review and editing.

Notes

The authors declare no competing financial interest.

■ REFERENCES

(1) Kulkarni, J. A.; Witzigmann, D.; Chen, S.; Cullis, P. R.; van der Meel, R. Lipid nanoparticle technology for clinical translation of siRNA therapeutics. *Accounts of chemical research* **2019**, *52*, 2435−2444.

(2) Kolate, A.; Baradia, D.; Patil, S.; Vhora, I.; Kore, G.; Misra, A. PEG—A versatile conjugating ligand for drugs and drug delivery systems. *Journal of controlled release* **2014**, *192*, 67−81.

(3) Hatakeyama, H.; Akita, H.; Harashima, H. The polyethylene-glycol dilemma: advantage and disadvantage of PEGylation of liposomes for systemic genes and nucleic acids delivery to tumors. *Biol. Pharm. Bull.* **2013**, *36*, 892−899.

(4) Verhoef, J. J.; Anchordoquy, T. J. Questioning the use of PEGylation for drug delivery. *Drug delivery and translational research* **2013**, *3*, 499−503.

(5) Zhang, P.; Sun, F.; Liu, S.; Jiang, S. Anti-PEG antibodies in the clinic: Current issues and beyond PEGylation. *J. Controlled Release* **2016**, *244*, 184−193.

(6) Narváez-Narváez, D. A.; Duarte-Ruiz, M.; Jiménez-Lozano, S.; Moreno-Castro, C.; Vargas, R.; Nardi-Ricart, A.; García-Montoya, E.; Pérez-Lozano, P.; Suñé-Negre, J. M.; Hernández-Munain, C.; Suñé, C.; Suñé-Pou, M. Comparative Analysis of the Physicochemical and Biological Characteristics of Freeze-Dried PEGylated Cationic Solid Lipid Nanoparticles. *Pharmaceuticals* **2023**, *16*, 1583.

(7) López-Estevez, A. M.; Gref, R.; Alonso, M. J. A journey through the history of PEGylated drug delivery nanocarriers. *Drug Delivery and Translational Research* **2024**, *14*, 2026−2031.

(8) Korake, S.; Bothiraja, C.; Pawar, A. Design, development, and in-vitro/in-vivo evaluation of docetaxel-loaded PEGylated solid lipid nanoparticles in prostate cancer therapy. *Eur. J. Pharm. Biopharm.* **2023**, *189*, 15−27.

(9) Tenchov, R.; Sasso, J. M.; Zhou, Q. A. PEGylated lipid nanoparticle formulations: immunological safety and efficiency perspective. *Bioconjugate Chem.* **2023**, *34*, 941−960.

(10) Kozma, G. T.; Shimizu, T.; Ishida, T.; Szebeni, J. Anti-PEG antibodies: Properties, formation, testing and role in adverse immune reactions to PEGylated nano-biopharmaceuticals. *Advanced drug delivery reviews* **2020**, *154*, 163−175.

(11) Estape Senti, M.; de Jongh, C. A.; Dijkxhoorn, K.; Verhoef, J. J.; Szebeni, J.; Storm, G.; Hack, C. E.; Schiffelers, R. M.; Fens, M. H.; Boross, P. Anti-PEG antibodies compromise the integrity of PEGylated lipid-based nanoparticles via complement. *J. Controlled Release* **2022**, *341*, 475−486.

(12) Zalba, S.; Ten Hagen, T. L.; Burgui, C.; Garrido, M. J. Stealth nanoparticles in oncology: Facing the PEG dilemma. *J. Controlled Release* **2022**, *351*, 22−36.

(13) Yang, H.; Wang, J.; Zhou, X.; Fu, D.; Le, C.; Wei, J.; Qian, Y.; Fang, Y.; Jin, T.; Kong, X.; Yu, C.; Song, D.; Wang, Y.; Zhou, X.; Zhou, T.; Zhou, Q.; Liu, X.; Xiao, Q.; Ding, K. Impact of protein corona and PEGylation on the accumulation and efficacy of lysosome-disrupting lipid nanoparticles in KRAS-mutated cancer. *Nano Today* **2024**, *56*, 102307.

(14) Adir, O.; Poley, M.; Chen, G.; Froim, S.; Krinsky, N.; Shklover, J.; Shainsky-Roitman, J.; Lammers, T.; Schroeder, A. Integrating artificial intelligence and nanotechnology for precision cancer medicine. *Adv. Mater.* **2020**, *32*, 1901989.

(15) Gilleron, J.; Querbes, W.; Zeigerer, A.; Borodovsky, A.; Marsico, G.; Schubert, U.; Manygoats, K.; Seifert, S.; Andree, C.; Stoter, M.; Epstein-Barash, H.; Zhang, L.; Koteliansky, V.; Fitzgerald, K.; Fava, E.; Bickle, M.; Kalaidzidis, Y.; Akinc, A.; Maier, M.; Zerial, M. Image-based analysis of lipid nanoparticle−mediated siRNA delivery, intracellular trafficking and endosomal escape. *Nature biotechnology* **2013**, *31*, 638−646.

(16) Coppola, S.; Pozzi, D.; De Sanctis, S. C.; Digman, M.; Gratton, E.; Caracciolo, G. Quantitative measurement of intracellular transport of nanocarriers by spatio-temporal image correlation spectroscopy. *Methods and applications in fluorescence* **2013**, *1*, 015005.

(17) Coppola, S.; Estrada, L. C.; Digman, M. A.; Pozzi, D.; Cardarelli, F.; Gratton, E.; Caracciolo, G. Intracellular trafficking of cationic liposome−DNA complexes in living cells. *Soft Matter* **2012**, *8*, 7919−7927.

(18) Digiacomo, L.; Digman, M. A.; Gratton, E.; Caracciolo, G. Development of an image Mean Square Displacement (iMSD)-based method as a novel approach to study the intracellular trafficking of nanoparticles. *Acta biomaterialia* **2016**, *42*, 189−198.

(19) Resina, S.; Prevot, P.; Thierry, A. R. Physico-chemical characteristics of lipoplexes influence cell uptake mechanisms and transfection efficacy. *PLoS One* **2009**, *4*, No. e6058.

(20) Giulimondi, F.; Digiacomo, L.; Pozzi, D.; Palchetti, S.; Vulpis, E.; Capriotti, A. L.; Chiozzi, R. Z.; Lagana, A.; Amenitsch, H.; Masuelli, L.; Peruzzi, G.; Mahmoudi, M.; Screpanti, I.; Zingoni, A.; Caracciolo, G. Interplay of protein corona and immune cells controls blood residency of liposomes. *Nat. Commun.* **2019**, *10*, 1−11.

(21) Giulimondi, F.; Vulpis, E.; Digiacomo, L.; Giuli, M. V.; Mancusi, A.; Capriotti, A. L.; Laganà, A.; Cerrato, A.; Zenezini Chiozzi, R.; Nicoletti, C.; Amenitsch, H.; Cardarelli, F.; Masuelli, L.; Bei, R.; Screpanti, I.; Pozzi, D.; Zingoni, A.; Checquolo, S.; Caracciolo, G. Opsonin-Deficient Nucleoproteic Corona Endows UnPEGylated Liposomes with Stealth Properties In Vivo. *ACS Nano* **2022**, *16*, 2088−2100.

(22) Rädler, J. O.; Koltover, I.; Salditt, T.; Safinya, C. R. Structure of DNA-cationic liposome complexes: DNA intercalation in multi-lamellar membranes in distinct interhelical packing regimes. *Science* **1997**, *275*, 810−814.

(23) Caracciolo, G.; Pozzi, D.; Caminiti, R.; Marchini, C.; Montani, M.; Amici, A.; Amenitsch, H. Enhanced transfection efficiency of multicomponent lipoplexes in the regime of optimal membrane charge density. *J. Phys. Chem. B* **2008**, *112*, 11298−11304.

(24) Akita, H.; Kudo, A.; Minoura, A.; Yamaguti, M.; Khalil, I. A.; Moriguchi, R.; Masuda, T.; Danev, R.; Nagayama, K.; Kogure, K.; Harashima, H. Multi-layered nanoparticles for penetrating the endosome and nuclear membrane via a step-wise membrane fusion process. *Biomaterials* **2009**, *30*, 2940−2949.

(25) Varga, Z.; Berényi, S.; Szokol, B.; Őrfi, L. s.; Kéri, G. r.; Peták, I.; Hoell, A.; Bóta, A. A closer look at the structure of sterically stabilized liposomes: a small-angle X-ray scattering study. *J. Phys. Chem. B* **2010**, *114*, 6850−6854.

(26) Varga, Z.; Wacha, A.; Vainio, U.; Gummel, J.; Bóta, A. Characterization of the PEG layer of sterically stabilized liposomes: a SAXS study. *Chem. Phys. Lipids* **2012**, *165*, 387−392.

(27) Schilt, Y.; Berman, T.; Wei, X.; Barenholz, Y.; Raviv, U. Using solution X-ray scattering to determine the high-resolution structure and morphology of PEGylated liposomal doxorubicin nanodrugs. *Biochimica et Biophysica Acta (BBA)-General Subjects* **2016**, *1860*, 108−119.

(28) Di Rienzo, C.; Gratton, E.; Beltram, F.; Cardarelli, F. Fast spatiotemporal correlation spectroscopy to determine protein lateral diffusion laws in live cell membranes. *Proc. Natl. Acad. Sci. U. S. A.* **2013**, *110*, 12307−12312.

(29) Digiacomo, L.; D'Autilia, F.; Durso, W.; Tentori, P. M.; Caracciolo, G.; Cardarelli, F. Dynamic fingerprinting of sub-cellular nanostructures by image mean square displacement analysis. *Sci. Rep* **2017**, *7*, 14836.

(30) Gaidarov, I.; Santini, F.; Warren, R. A.; Keen, J. H. Spatial control of coated-pit dynamics in living cells. *Nature cell biology* **1999**, *1*, 1−7.

(31) Wang, Z.; Tiruppathi, C.; Minshall, R. D.; Malik, A. B. Size and dynamics of caveolae studied using nanoparticles in living endothelial cells. *ACS Nano* **2009**, *3*, 4110−4116.

(32) De Maesschalck, R.; Jouan-Rimbaud, D.; Massart, D. L. The mahalanobis distance. *Chemometrics and intelligent laboratory systems* **2000**, *50*, 1−18.

(33) Skotland, T.; Iversen, T. G.; Sandvig, K. Cellular uptake of nanoparticles: Involvement of caveolae? *Precision Nanomedicine* **2021**, *4*, 782−786.